International Journal for Numerical Methods in Biomedical Engineering

WILEY

APPLIED RESEARCH OPEN ACCESS

Modeling Hemodynamic Effects of the Closure Procedure of Carotid Artery Endarterectomy

Laurel Morgan Miller Marsh[1] | Rainald Löhner[1] | Tatiana Abou-Mrad[2] | Laura Stone McGuire[2] | Fady T. Charbel[2] | Juan Raul Cebral[1]

[1]Department of Bioengineering, George Mason University, Fairfax, Virginia, USA | [2]Department of Neurosurgery, University of Illinois Chicago, Chicago, Illinois, USA

Correspondence: Juan Raul Cebral (jcebral@gmu.edu)

Received: 4 September 2024 | **Revised:** 23 April 2025 | **Accepted:** 10 May 2025

Funding: This work was supported by Travis C. Valentine Memorial.

Keywords: computational fluid dynamics | patch angioplasty | primary closure | restenosis

ABSTRACT

Currently, it is unclear why some patients experience restenosis after carotid endarterectomy (CEA) and whether the closing procedure is linked to greater rates of restenosis. Here, the morphology and hemodynamics are compared for the carotid bulb of two patients post-CEA. One carotid bulb was closed with a patch which later suffered a restenosis, while the other patient's bulb was treated using primary closure and did not. Contrast-enhanced magnetic resonance angiography (CE-MRA) was segmented to provide the domain for computational fluid dynamics (CFD). Flowrate waveforms measured with phase-contrast MR were provided for the common carotid artery (CCA) and internal carotid artery (ICA), while only the mean flow rate was provided for the external carotid artery (ECA), requiring the ECA waveform to be calculated. A Womersley profile was applied to the CCA inlet and ECA outlet, with a traction-free boundary condition applied to the ICA outlet. The patch patient who restenosed exhibited a nonphysiological hemodynamic environment that differed from the flow environment observed in the healthy, contralateral bulb. In contrast, the hemodynamics of the primary closure patient who underwent a successful CEA showed more favorable levels and trends of WSS as well as healthy mixing from vortices that were both present in the healthy, contralateral bulb. Changing model parameters such as flow rate, wall compliance, and flow waveforms did not alter these conclusions. Therefore, the geometry of the carotid bulb, as opposed to flow characteristics, seems responsible for the observed differences between these two cases in hemodynamic environments and subsequent outcomes.

1 | Introduction

Stenosis of the carotid artery can be treated by carotid endarterectomy (CEA), the focus of this study, or endovascularly by balloon angioplasty either with or without stenting. Yet, successful procedures remain at risk of restenosis, the cause of which is still debated. The mechanism of restenosis is thought to be either myointimal hyperplasia if recurrence is within 36 months or, as this study focuses on, continued atherosclerosis for longer-term restenosis [1]. The risk of recurrence is thought to be tied to the closing procedure. Primary closure involves directly suturing the carotid bulb. Due to the risk of restenosis, patch angioplasty was later introduced, which involves suturing a patch to the edges of the incision, thereby attempting to reconstruct the bulb's original geometry [2]. While one Cochrane review has shown that patch angioplasty reduces the risk of restenosis [3], there is still no final consensus on whether using a patch will decrease the chance of restenosis in either literature or clinical practice, as primary closure is still often performed [4, 5].

Healthy and disturbed flow within the carotid bulb has been extensively studied. The carotid bulb is located at the

bifurcation of the common carotid artery (CCA) into the internal carotid artery (ICA) and external carotid artery (ECA). At its most proximal end, the ICA experiences a dilation that defines the carotid bulb. At wall shear stress (WSS) values of 15 dyne/cm^2 or greater, endothelial cells exhibit atheroprotective phenotypes, while endothelial cells experiencing WSS < 4 dyne/cm^2 exhibit proatherogenic phenotypes [6]. Studies have assessed typical WSS in the carotid and in the bulb directly, finding WSS values closer to the 4 dyne/cm threshold in the bulb [7, 8]. The area of the wall opposite the apex of the bifurcation is where this low WSS is found to be localized, while the wall near the bifurcation experiences physiological levels of shear standard for arteries [7]. Since low WSS and high oscillatory shear index (OSI) have been implicated in the development of atherosclerosis [6, 9], the low shear area of the bulb is a region of interest, particularly if paired with high OSI [10]. Furthermore, this tendency of low WSS and high OSI leading to thickening walls has been, like many other hemodynamic parameters in the ICA bulb, correlated to bifurcation morphology [11]. Many WSS-based hemodynamic studies of the carotid bifurcation have focused on low WSS paired with high OSI [10, 12, 13]; however, high WSS gradients have also been implicated in other cerebrovascular pathologies [14].

Along with these WSS patterns, vortex pairs have been identified in the ICA bulb and are characterized by the vessel curvature, radius, and flow velocity [7]. These vortices are one component thought to contribute to healthy mixing of blood and are seen throughout certain nonpathological bifurcations within the vasculature [15, 16]. Although the geometry of the carotid bulb has been shown to be associated with increased flow disturbance [17], the patch closing approach of CEA intends to restore the original geometry of the bulb and as such leaves both a more tapering and a tortuous bulb when compared to other closing methods, including primary closure [12, 18, 19]. So while the disturbed flow and low WSS regions, known to be associated with endothelial dysfunction, wall inflammation, and NF-kB activation [6, 20], may lead to a negative outcome, in some cases this may be mitigated by the effects of swirling and mixing flow.

Here, we apply computational fluid dynamics (CFD) to determine and compare the hemodynamics of two intriguing post-CEA cases, one with a patch closure that later restenosed and the other with a primary closure that remained successful.

2 | Methods

2.1 | Vascular Modeling

Data from two patients treated with CEA were used to build corresponding CFD models. A patch graft was used to close patient 1 (Pt 1) who suffered a stroke due to restenosis 8 years after the intervention. Primary closure was used on patient 2 (Pt 2) who did not experience any morbidity or restenosis upon follow-up. Contrast-enhanced magnetic resonance angiography (CE-MRA) taken immediately after the CEA interventions (and again after restenosis for Pt1) was used to build corresponding patient-specific vascular models. These images consisted of a stack of 152 slices of 512 × 512 pixels, with an in-plane resolution of 0.332 and 0.7 mm slice thickness.

The left (healthy) and right (treated) carotid arteries bifurcations of both patients were segmented using Amira (v6.2.0, Thermo Fisher Scientific Inc., Waltham, Massachusetts). The models included a portion of the CCA, the ECA, and the ICA including the bulb. The surface triangulations of the reconstructed vascular models were then smoothed, optimized, and truncated perpendicularly to the vessel axis using in-house software [21]. Next, unstructured, tetrahedral meshes were generated using an advancing-front method implemented in an in-house grid generator [21]. The element size was 0.2 mm, resulting in meshes of approximately 4 million elements. Since viscous effects are important throughout the blood flow, not simply near the wall, this mesh resolution is uniform throughout the domain, which has been shown to produce accurate results [21, 22]. In addition, to improve the resolution near the wall and aid in the calculation of wall shear stress, a quadratic recovery of boundary gradients approach is applied [23].

2.2 | Flow Conditions

Using phase-contrast MR with 12 phases and a pixel size of 0.7–0.8 mm, mean flow rates were measured after the CEA intervention in both the left and the right carotids. Flow waveforms were reconstructed for the right CCA and ICA (treated side) using NOVA-Neuro software (ValSol Inc., Chicago, Illinois). Two cardiac cycles were averaged to create the CCA and ICA flow rates. The ECA flow rate waveform was calculated by first subtracting the mean flow rate of the ICA from the CCA and then scaling the ICA or CCA flow rate to produce a waveform for the ECA that satisfied time-averaged mass conservation at the carotid bifurcation:

$$< Q_{\mathrm{ECA}} > = < Q_{\mathrm{CCA}} > - < Q_{\mathrm{ICA}} > \tag{1}$$

$$Q_{\mathrm{ECA}} = Q_{\mathrm{xCA}} \frac{< Q_{\mathrm{ECA}} >}{< Q_{\mathrm{xCA}} >} \tag{2}$$

where Q is the flowrate, <> represents the mean (time average over the cardiac cycle), and xCA indicates either the ICA or CCA. This approach implies that the instantaneous difference in flow rates of the CCA (inflow) and the ICA and ECA (outflows) is due to the motion of the compliant vascular. If the vessel walls are assumed rigid, the instantaneous ECA flowrate is directly computed as the instantaneous difference of the CCA and ICA flowrates: $Q_{\mathrm{ECA}}(t) = Q_{\mathrm{CCA}}(t) - Q_{\mathrm{ICA}}(t)$.

The only available flow data for the left carotids were the mean flow rates of the CCA and ICA. Hence, Equation (1) was applied to find $<Q_{\mathrm{ECA}}>$ of the left carotid. Then, the three flow rate waveforms for the right carotids (CCA, ICA, and ECA) were scaled by the left side's mean values with an equation similar to Equation (2). Unless noted, the ECA waveform was created by scaling the ICA waveform.

2.3 | Hemodynamics Modeling

The unsteady Navier–Stokes equations were numerically solved with an in-house finite element code [24] to simulate pulsatile, incompressible blood flow, which was modeled as Newtonian

fluid with a constant dynamic viscosity of $\mu = 0.04$ Poise and a density of $\rho = 1.105\,\mathrm{g/cm^3}$. Greater detail of segmentation, mesh, and simulation parameters can be found in [21].

Blood flow was simulated for the right carotid bifurcation (the side treated with CEA for both patients) as well as the healthy, left carotid bifurcation, for comparison. As mentioned above, since flowrate waveforms were only available for the right side, these waveforms were scaled to the appropriate mean flowrate values and applied to the left side. A Womersley velocity profile was then applied to the CCA inlet and ECA outlet [21]. The ICA outlet was modeled as a traction-free boundary condition. Vessel walls were first approximated as rigid, and no-slip boundary conditions were applied at the walls.

2.4 | Vessel Wall Compliance

To investigate how the motion of the vessel wall due to its compliance might affect the results of this study, a uniform pulsatile velocity was applied at the vessel wall for each case and compared to the motionless rigid version. The instantaneous wall velocity was determined using the NOVA data and calculated ECA flowrate as shown below:

$$Q_{\mathrm{wall}}(t) = Q_{\mathrm{CCA}}(t) - Q_{\mathrm{ICA}}(t) - Q_{\mathrm{ECA}}(t) \tag{3}$$

$$\mathrm{Velocity}_{\mathrm{wall}} = \frac{Q_{\mathrm{wall}}}{\mathrm{Area}_{\mathrm{wall}}} \tag{4}$$

This velocity (which has zero-mean) was prescribed at the vessel wall in the normal direction, and the mesh was kept fixed.

2.5 | Data Analysis

2.5.1 | Geometric Parameters

In order to characterize the geometry of the bulb, vessel skeletons were constructed from the vascular models using in-house tools [25]. The skeleton consists of a set of points along the vessel centerline connected via edge segments (i.e., two node linear elements). At each skeleton point, the inner and outer radius of the vessel is given. The skeletons were produced through the CCA and into the bifurcation of the ECA and ICA. The centerline from the bifurcation (origin of the ICA) to 5 cm distal is then used to define the region of interest for each bulb. Then, the following morphological parameters were calculated for each ICA bulb: maximum tortuosity (path distance over Euclidean distance), mean eccentricity (outer over inner radius), mean width (average of inner and outer radius), and mean tapering (proximal over distal radius). These quantities were calculated at each point along the centerline and subsequently averaged over the bulb skeleton.

2.5.2 | Hemodynamic Parameters

The hemodynamic parameters used to compare the flow conditions in the two treated patients as well as their corresponding healthy sides are detailed below.

The wall shear stress vector $\boldsymbol{\tau_w}$ is defined as the tangential component of the shear stress vector evaluated at the vessel wall, $\boldsymbol{\tau}$:

$$\boldsymbol{\tau_w} = [\boldsymbol{\tau} - (\boldsymbol{\tau}\cdot\boldsymbol{n})\,\boldsymbol{n}\,]_{\mathrm{wall}} \tag{5}$$

where $\boldsymbol{n}$ is the unit vector normal to the wall. This is used to calculate the mean wall shear stress (WSS) and oscillatory shear index (OSI) for one cardiac cycle with a period of T, and averaged across the carotid bulb region:

$$\mathrm{WSS} = \frac{1}{T}\int_0^T |\,\boldsymbol{\tau_w}\,|\;dt \tag{6}$$

$$\mathrm{OSI} = \frac{1}{2}\left(1 - \frac{\left|\int_0^T \boldsymbol{\tau_w}\,dt\right|}{\int_0^T |\boldsymbol{\tau_w}|\,dt}\right) \tag{7}$$

The mean vorticity (VOR) is averaged over the carotid bulb then over one cardiac cycle:

$$\mathrm{VOR} = \frac{1}{T}\int_0^T |\nabla\times\boldsymbol{u}|\;dt \tag{8}$$

where $\boldsymbol{u}$ is the flow velocity vector.

Additionally, vortex corelines were identified in the bulb region using a previously described methodology [26] to visualize and quantify the swirling characteristics of the bulb flow pattern. The total length of the detected vortex corelines (CORELEN) was then computed and used as a metric of flow complexity and the amount of flow mixing.

Finally, the total kinetic energy (KE) of the flow within the bulb region was computed as:

$$\mathrm{KE} = \int \frac{1}{2}\rho|\boldsymbol{u}|^2 dV \tag{9}$$

and averaged over the cardiac cycle.

3 | Results

3.1 | Bulb Geometries and Flow Rates

The geometric characteristics of the left and right carotid bulbs of both patients are presented in Table 1. It can be seen that the bulb reconstructed with a patch (Pt1-Right-CEA patch) was wider with a larger mean radius, more eccentric, more tortuous, and with a larger tapering than the bulb reconstructed through primary closure without a patch (Pt2-Right-CEA no patch). After it restenosed, the mean radius of this bulb decreased while its tapering increased.

The mean flow rates measured with phase-contrast MR in the left and right CCAs and ICAs of both patients are presented in

TABLE 1 | Geometric characteristics of the left (healthy) and right (CEA treated) carotid bulbs of both patients.

Patient	Bulb	Radius (mm)	Eccentricity	Tortuosity	Tapering
Pt1	Left (healthy)	2.8	1.48	1.50	2.87
	Right (CEA patch)	3.4	1.42	1.31	3.24
	Right (restenosed)	3.0	1.25	1.31	3.40
Pt2	Left (healthy)	2.9	1.15	1.09	1.60
	Right (CEA no patch)	2.2	1.26	1.15	3.00

TABLE 2 | Mean flow rates measured with phase-contrast MR.

Patient	Bulb	$< Q_{CCA} >$ (cc/s)	$< Q_{ICA} >$ (cc/s)
Pt1	Left (healthy)	4.75	3.43
	Right (CEA patch)	4.2	3.32
Pt2	Left (healthy)	11.4	3.08
	Right (CEA no patch)	9.23	2.75

Table 2. The corresponding flow waveforms obtained on the right CCAs and ICAs of each patient are presented in Figure 1 (top row). This figure also shows the calculated ECA flow curves, as well as the vessel wall velocities calculated as explained in Sections 2.2 and 2.4. Although patient 1 had lower mean flow rates in the CCAs than patient 2, the flows in the ICAs were similar. The larger difference between flow rates in the CCA and ICA of patient 2 results in a larger wall velocity in this case, possibly indicative of a more compliant vessel in this patient.

3.2 | Patch Versus Primary Closure

Values of the hemodynamic parameters calculated over the left and right bulb regions of each patient are presented in Table 3. It can be seen that compared to the primary closure, the patch closure resulted in lower WSS, larger OSI (more oscillatory flow), lower vorticity (less fluid rotation), shorter vortex corelines (less flow swirling), and lower kinetic energy (slower flow). In the case without patch closure, the hemodynamic environment was more physiologic, with physiologic values of WSS, faster flow, and substantial rotation and swirling that typically induces more blood mixing along the vessel.

Visualizations of the hemodynamic environment in the right bulb of patient 1 are presented in Figure 2. Corresponding visualizations for patient 2 are presented in Figure 3. These figures show the WSS magnitude (top row), instantaneous flow streamlines (middle row), and vortex corelines (bottom row) at four selected instants during the cardiac cycle (indicated in the inserts of the bottom row). These visualizations clearly show a low flow environment in the bulb of patient 1, with low WSS throughout the entire bulb, and very little swirling with only some vortex corelines detected during the diastolic phase. In contrast, patient 2 had higher WSS values and substantial swirling during the entire systolic phase. The streamline visualizations also provide a sense of the mixing along the bulb of patient 2, while for patient 1 they run in a more parallel fashion. Additionally, it can be seen that in patient 1, there was a gradient of WSS at the distal part of the bulb where the WSS went from the low WSS values in the bulb to much higher values in the distal ICA, and this gradient was persistent throughout the cardiac cycle. In patient 2, although there were regions of low WSS and high WSS in the bulb, the gradients were a bit more diffuse and changed during the cardiac cycle. In this case, WSS values fluctuated throughout the cycle, producing a sweeping gradient that covered most of the carotid bifurcation with no intense gradients for a particular region.

Comparisons of the OSI distributions are presented in Figure 4. It can be seen that in both cases there are regions of elevated OSI. In patient 1, this high OSI region was located toward the side/posterior wall of the bulb where the WSS was low. In patient 2, the high OSI region was located at the posterior wall of the bulb where the WSS reached physiologic levels, although not uniformly. Perhaps this bulb could be protected from atherosclerotic effects in this area of high OSI by the exposure to elevated WSS levels that occurred around systole.

3.3 | Reconstructed Versus Healthy Bulbs

Compared to the healthy side (see Table 3 and Figure 5), the CEA treated bulb of patient 1 (with patch closure) had lower WSS and higher OSI, lower vorticity and kinetic energy, but larger vortex corelines. The larger coreline length was mainly associated with flow recirculation toward the proximal origin of the bulb rather than with swirling flow along the bulb (see Figure 2). In summary, the healthy side had physiologic levels of WSS with little oscillation produced by faster flow with almost no swirling and modest fluid rotation. Even though there was a region of elevated WSS at the distal end of the left bulb, the bulb itself was exposed to higher levels of WSS than in the right side, which resulted in a

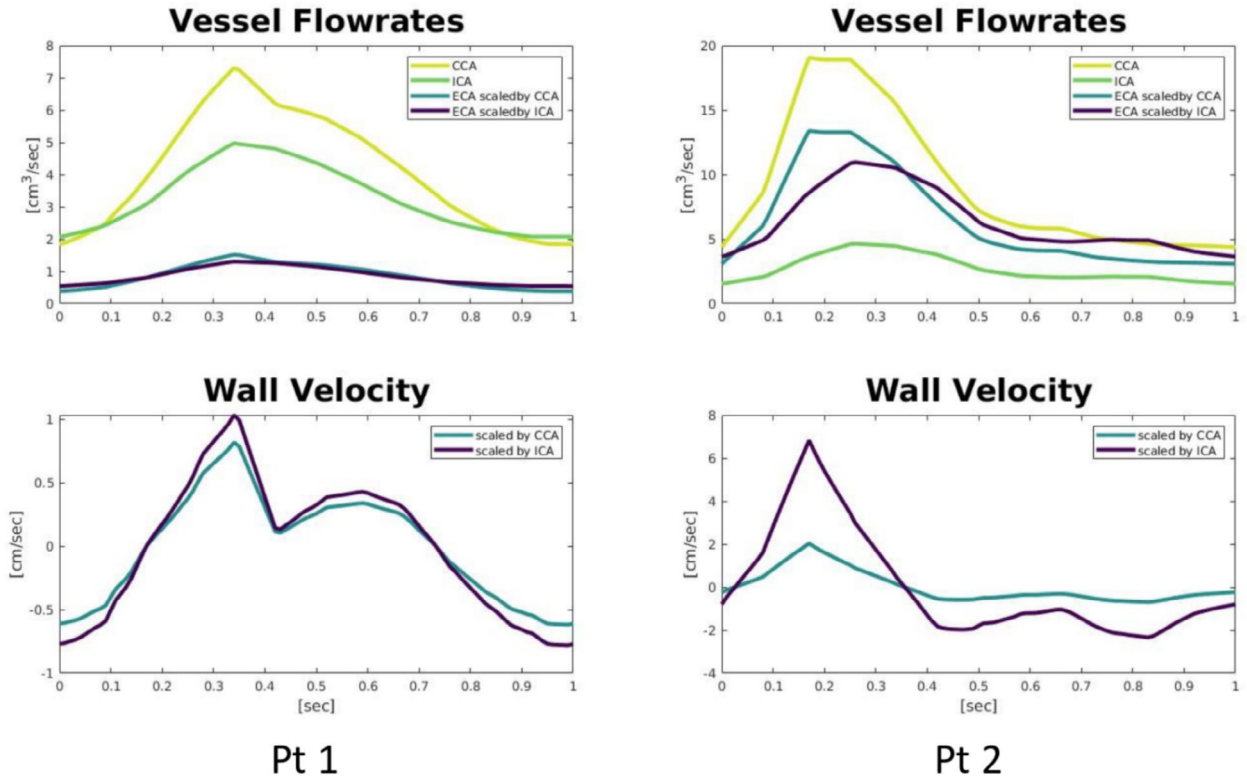

FIGURE 1 | Flow waveforms measured in the right CCA and ICA of each patient and calculated ECA flow curves (top row), along with calculated vessel wall velocities (bottom row).

TABLE 3 | Hemodynamic variables computed over the bulb region of both patients.

Patient	Bulb	WSS (dyne/cm^2)	OSI	VOR (1/s)	CORELEN (cm)	KE (erg)
Pt1	Left (healthy)	13.4	0.007	119.0	0.03	263.0
	Right (CEA patch)	5.99	0.045	48.8	2.10	73.9
	Right (restenosed)	3.6	0.008	31.8	1.87	22.3
Pt2	Left (healthy)	25.9	0.066	255.0	2.65	814.0
	Right (CEA no patch)	29.5	0.007	277.0	3.20	786.0

more gradual transition or WSS gradient. Thus, the patch closure was unable to produce a hemodynamic environment similar to the one observed on the contralateral healthy side.

In contrast, in the case of patient 2, the CEA with primary closure resulted in an overall hemodynamic environment similar to the one on the healthy side (see Table 3 and Figure 6). In this case, the healthy and CEA-reconstructed bulbs both had physiological levels of WSS, faster flows, substantial fluid rotation, and persistent swirling.

The distributions of OSI in the healthy left bulbs of patients 1 and 2 are presented in Figure 7. In patient 1, the OSI was low throughout the bulb, while in patient 2 it was higher, but the regions of elevated OSI concentrated toward the origin and back wall of the bulb, which were exposed to elevated WSS during parts of the cardiac cycle. In patient 1, the CEA reconstruction with patch closure resulted in an increase of OSI (in a region of low WSS), while in patient 2 the CEA with primary closure resulted in a decrease of OSI.

3.4 | Effect of Restenosis

As mentioned before, 8 years after CEA treatment of the right carotid of patient 1 using a patch closure, the patient suffered a stroke, and the artery was found to be restenosed. Figure 8 shows the peak systole WSS and OSI immediately after the CEA reconstruction and at follow-up after it restenosed. The restenosis regions indicated in the figure coincide with exposure to low WSS and high OSI (green oval toward the proximal bulb origin) and to large WSS gradient (purple oval toward the distal end of the bulb). Once the bulb restenosed, the WSS in the bulb became even lower, but the high WSS gradient at the distal end was maintained (it actually moved to a slightly more proximal location) and the region of high OSI enlarged.

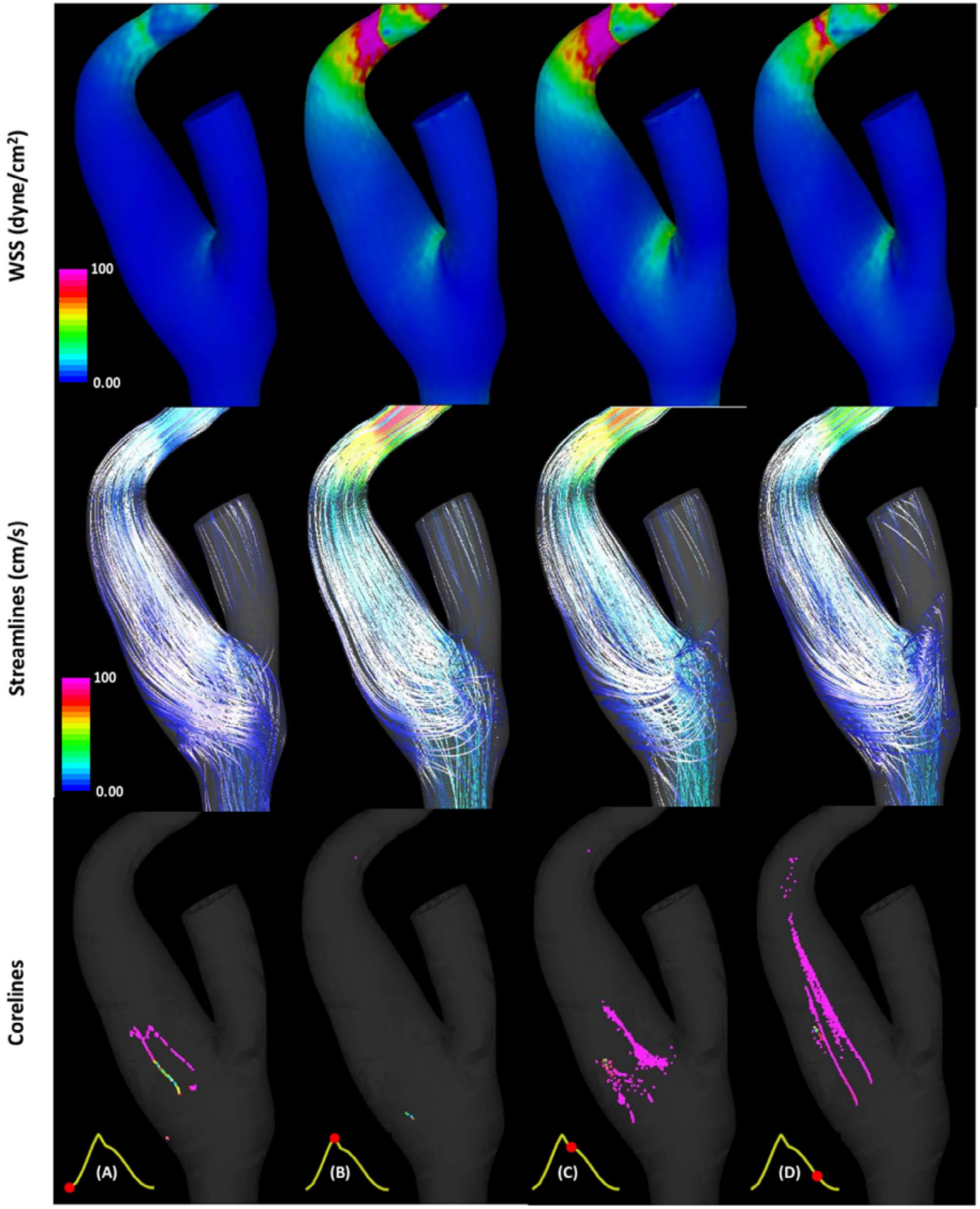

FIGURE 2 | Flow visualization in the right bulb of patient 1 (after CEA with patch).

Additionally (see Table 3 and Figure 9), the vorticity, swirling, and flow velocity decreased, and the transient vortices observed toward the proximal origin of the bulb were associated with a flow recirculation region created in this area and not with swirling along the bulb. In summary, the restenosis of the CEA treated bulb exacerbated the unfavorable hemodynamic conditions that promote further atherosclerotic progression and/or thrombus formation potentially causing embolic events.

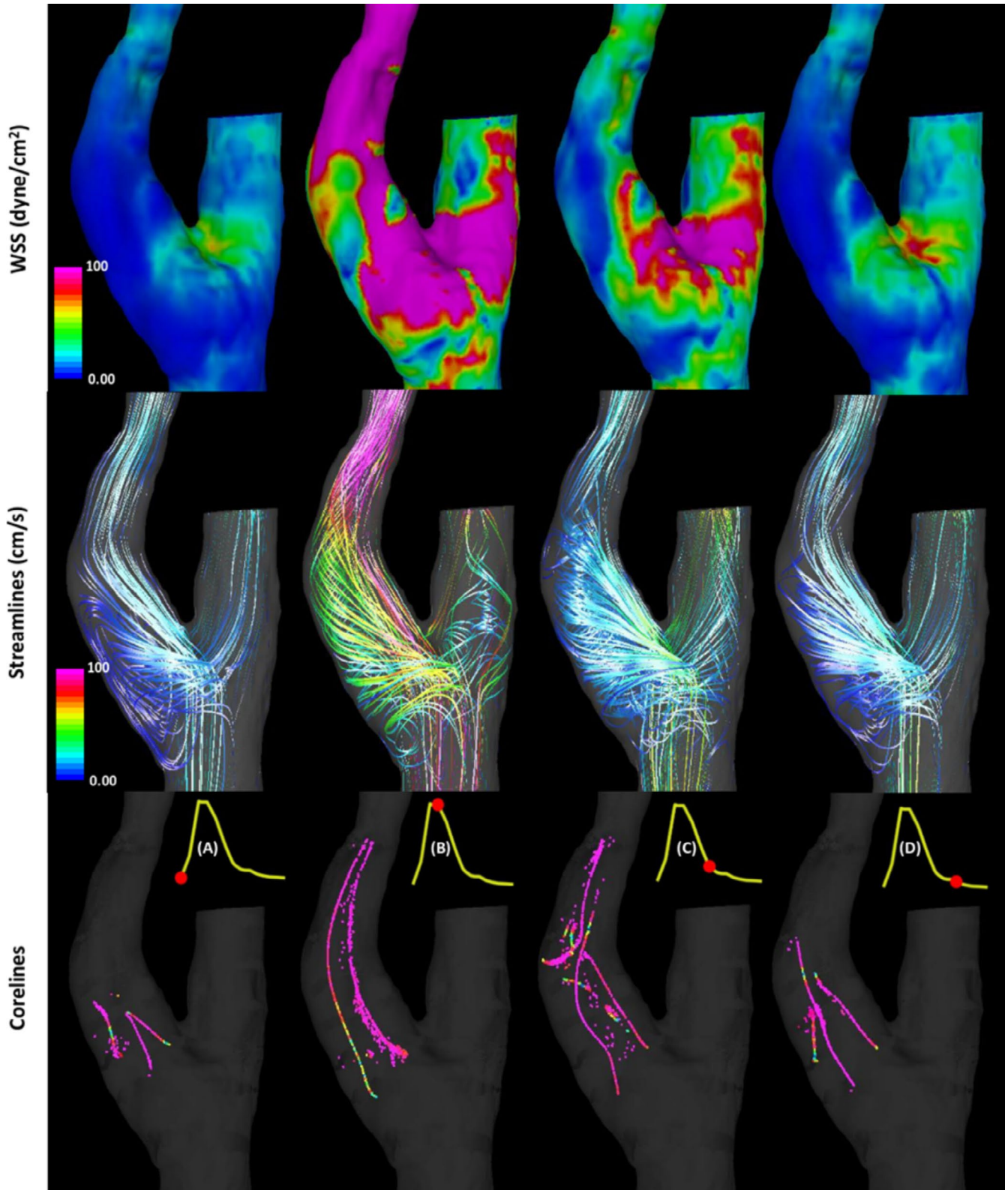

FIGURE 3 | Flow visualization in the right bulb of patient 2 (after CEA without patch).

3.5 | Sensitivity to Flow Rates

As can be seen in Table 2, in both patients, the treated side had lower flows than in the contralateral healthy sides. Therefore, in order to study the influence of the flow rates and to investigate whether the differences observed between the patch and the primary closures are due to the geometry of the reconstructed bulbs or the different flow rates, simulations of the right (treated) side were carried out by imposing the flow rates measured on the left (healthy) side. The corresponding changes in the hemodynamic parameters are presented in Table 4. It can be seen that in patient 1, which had larger flow rates in the ICA

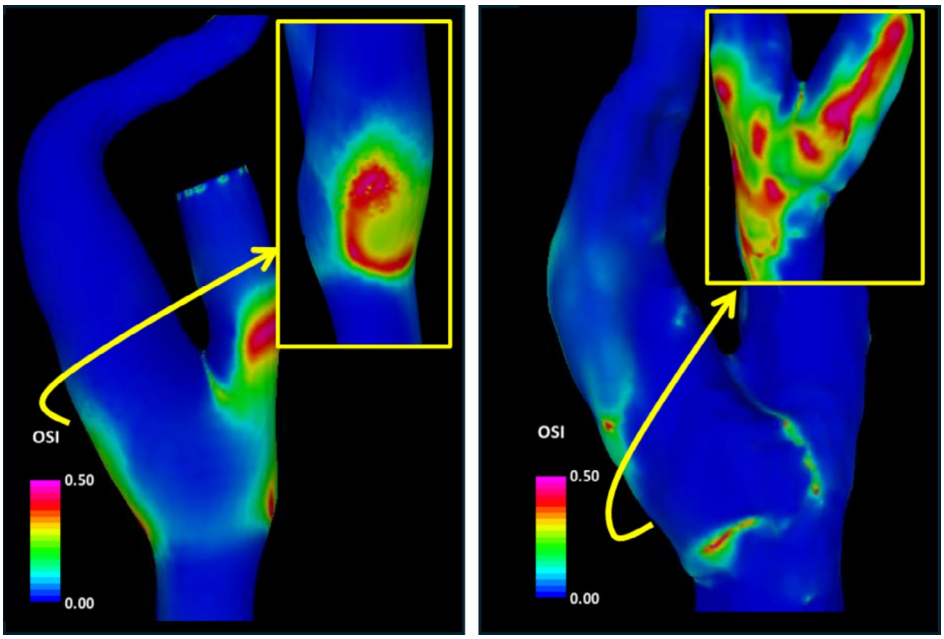

FIGURE 4 | Oscillatory shear index (OSI) in the right bulb of patient 1 (left) and patient 2 (right). Inserts show the exterior (Pt1) and posterior wall (Pt2) of the carotid bulb.

than patient 2, the changes were quite small, only a slight increase in kinetic energy and vortex coreline length. In patient 2, changes were more significant, but in this case, the WSS, vorticity, vortex coreline length, and kinetic energy increased while OSI decreased. As such, the differences observed between the patch and primary closures are even more pronounced, and it can be concluded that they are mainly the result of the different bulb geometries and not because of differences in the flow rates.

3.6 | Sensitivity to Wall Compliance

Relative changes in the hemodynamic variables obtained with the compliant models (i.e., with a nonzero wall velocity) with respect to the rigid wall models are presented in Table 5. It can be seen that in general, the compliant models yield lower values of the hemodynamic parameters compared to the rigid wall models. Vorticity and WSS were the least sensitive to wall motion. As expected, OSI and KE experienced larger changes, especially for patient 2, which had larger wall velocities (i.e., presumably more compliant vessels). Interestingly, the moving walls reduced the vortex coreline length, indicating that with compliant walls there was less swirling of the flow, especially for the case with patch (patient 1). Nevertheless, the overall distribution of hemodynamic variables and flow structures was consistent between the compliant and rigid models, as illustrated in Figure 10 with patient 2, which encompasses the largest changes. This indicates that using compliant models would not change the conclusions of comparisons between CEA with and without patch.

3.7 | Sensitivity to Flow Waveform

As explained before, the flow waveforms in the ECAs were not available, and thus, the ECA flow curves were obtained by scaling either the ICA (default) or the CCA waveforms to conserve the mean flow rates. The changes in hemodynamic parameters obtained when employing the CCA waveform instead of the ICA waveform are presented in Table 6. Again, WSS and VOR were not substantially affected (changes below 10% for all cases), and larger changes were observed in OSI, CORELEN, and KE. Despite these numerical differences, the flow structures and overall hemodynamic parameter distributions remain unchanged, as shown in Figure 10. These observations also indicate that using ICA or CCA waveforms would not change the conclusions of comparisons between CEA with and without patch. Nevertheless, if ECA waveforms were measured in future studies, these uncertainties could be avoided.

Additionally, flow simulations were also performed by imposing steady flow boundary conditions corresponding to the mean flows measured in each artery. The changes obtained with steady flows compared to the mean values of hemodynamic parameters obtained with pulsatile flow conditions are presented in Table 7. Although changes in mean WSS and vorticity were relatively small, changes in kinetic energy and especially vortex coreline length were significantly larger. Furthermore, time-dependent parameters such as OSI cannot be obtained with steady flow simulations. As such, although steady flow simulations could provide a quick first analysis and estimations of mean hemodynamic variables, pulsatile simulations are more reliable and detailed and are recommended for future studies.

4 | Discussion

A patch closing procedure enables the restoration of the carotid bulb's original shape, while a primary closure tends to leave a smaller taper and less tortuous bulb [12, 18, 19]. Patient 1, closed by patch, did exhibit a larger taper and tortuosity than that of patient 2, primary closure. The taper and tortuosity of the bulb are thought to predict disturbed flow,

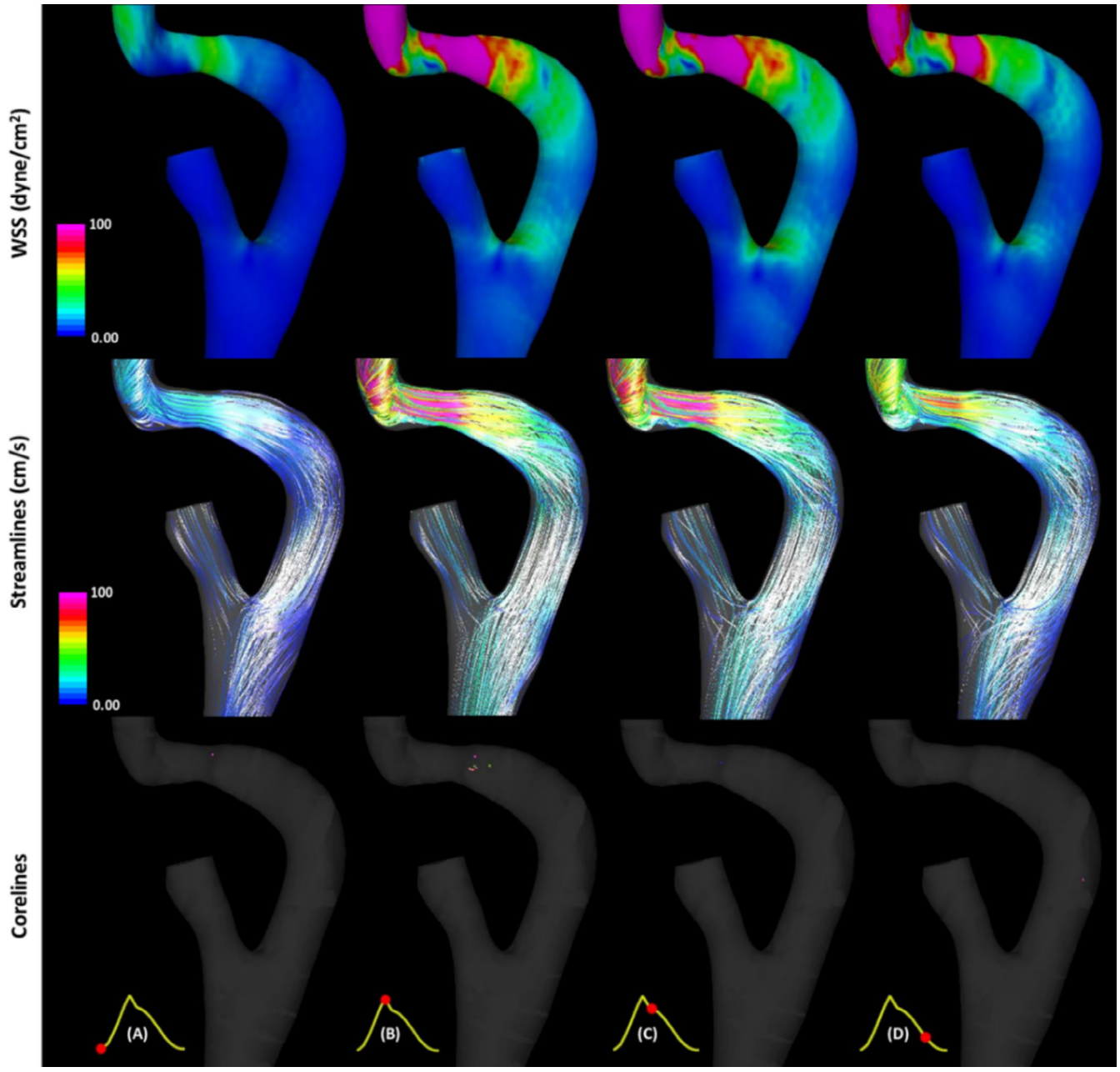

FIGURE 5 | Flow visualization in the left bulb of patient 1 (healthy).

described by WSS patterns [17], and the healthy mixing provided by vortex pairs depends on vessel curvature. Therefore, the geometry is clearly important for a healthy carotid bulb. However, this does not indicate that patch angioplasty itself is necessarily causing or preventing restenosis, simply that the bulb geometry that most often results from patching might be leading to undesirable hemodynamic environments in certain cases. As our concurrent study suggests (Abou-Mrad, 2025, *Journal of Neurosurgery: Case Lessons* [Accepted]), perhaps it is not simply the closing method that is to be considered, but more so the resulting bulb geometry and its corresponding hemodynamic environment.

In the present study, the patched carotid geometry did have the higher taper and tortuosity characteristics of this closing type. The hemodynamics reflected a nonphysiological environment with less mixing than in the primary closure patient. Two regions of disturbed flow based on WSS metrics corresponded to regions of restenosis. Interestingly, the healthy, contralateral side of patient 1 produced very little swirling but still experienced fluid rotation; however, this level of rotation was not recovered by the post-CEA patch geometry of the right side. Finally, the left bulb exhibited physiological levels of WSS with little oscillation that was not matched by the right side. While the right bulb of patient 2 created a physiological hemodynamic environment that was mirrored in the healthy, left bulb, hence, the primary closure produced a geometry that led to flows that were seen in the healthy, contralateral carotid and other healthy carotids [7].

To determine what flow-related changes had the most impact on the outcome of the hemodynamics, this study considered the effects of increased flow rates, wall compliance through

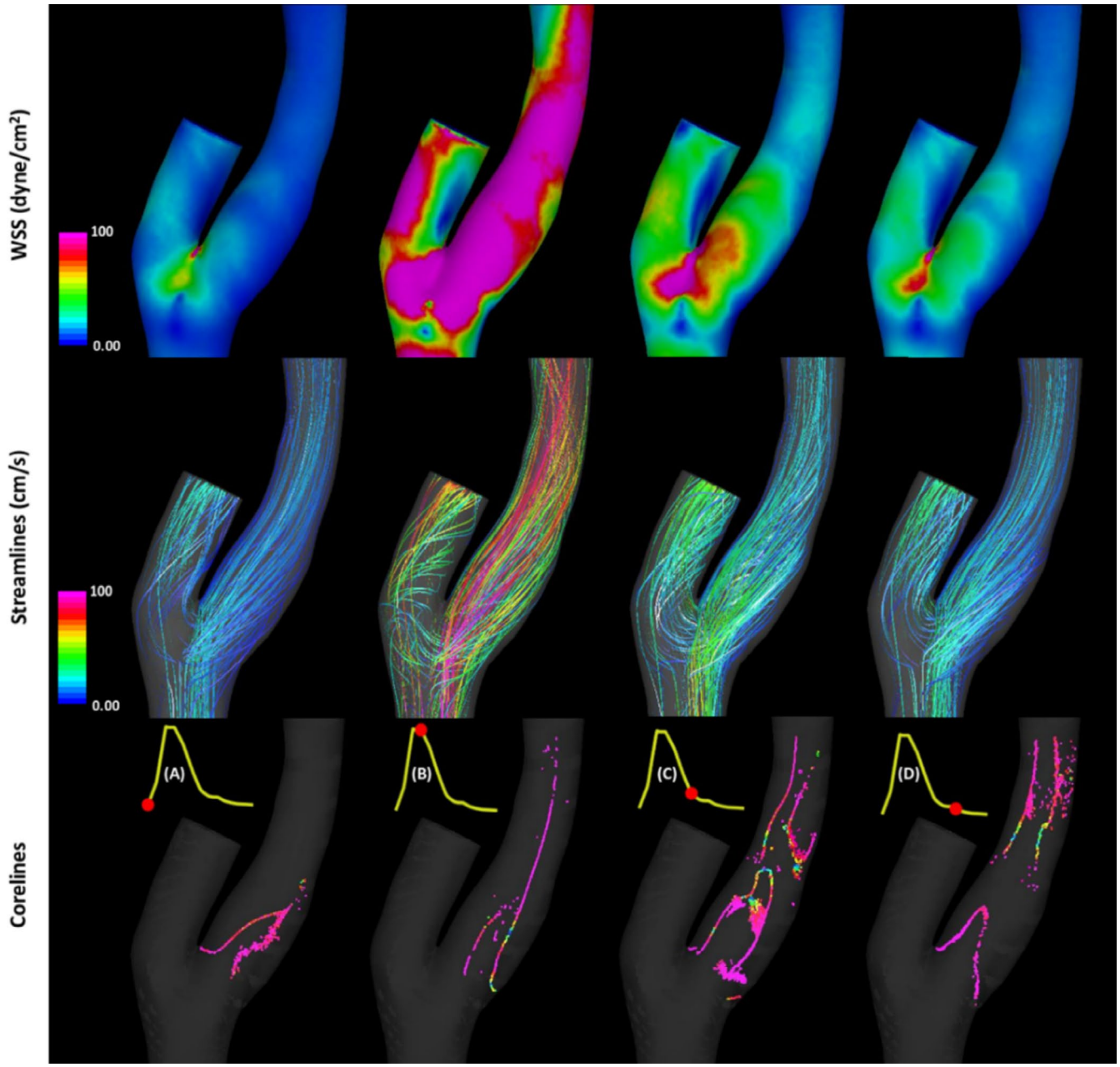

FIGURE 6 | Flow visualization in the left bulb of patient 2 (healthy).

the addition of a velocity imposed at the vessel wall, and applying distinct ECA waveforms. Steady state is not recommended, except for a speedy, initial analysis. The increase of patient 2's flow rate on the right side to match those of the healthy left side was greater than that of patient 1's leading to large changes in WSS, OSI, VOR, and KE. This produced the largest change in WSS, VOR, and KE from all of the flow-related changes. Considering wall compliance and altering the waveform most greatly affected OSI and CORELEN, and specifically for patient 2, KE. However, despite these quantitative differences, whether due to variations in flowrate, rigid wall versus compliant wall models, or differing waveforms, the hemodynamic environments, fluid structures, and WSS patterns remained fairly consistent. Importantly, the observed trends between patient 1 and 2 and their healthy, contralateral side remained regardless of these alterations. This indicates that the distinct hemodynamic outcomes are not driven by flow but the carotid bulb geometry.

In our study, we considered the hemodynamic environment created immediately after CEA and observed differences between two patients with different long-term outcomes, suggesting that perhaps these distinct flow conditions might have contributed to their different subsequent evolutions. The study did not consider the change in these conditions as the stenosis progressively developed. While providing interesting insight, this pilot study is constrained by the following limitations. Primarily, the small sample size restricts the generalizability of the findings; to move beyond our hypothesis here to clinical recommendations, a larger cohort is required. Material properties, including

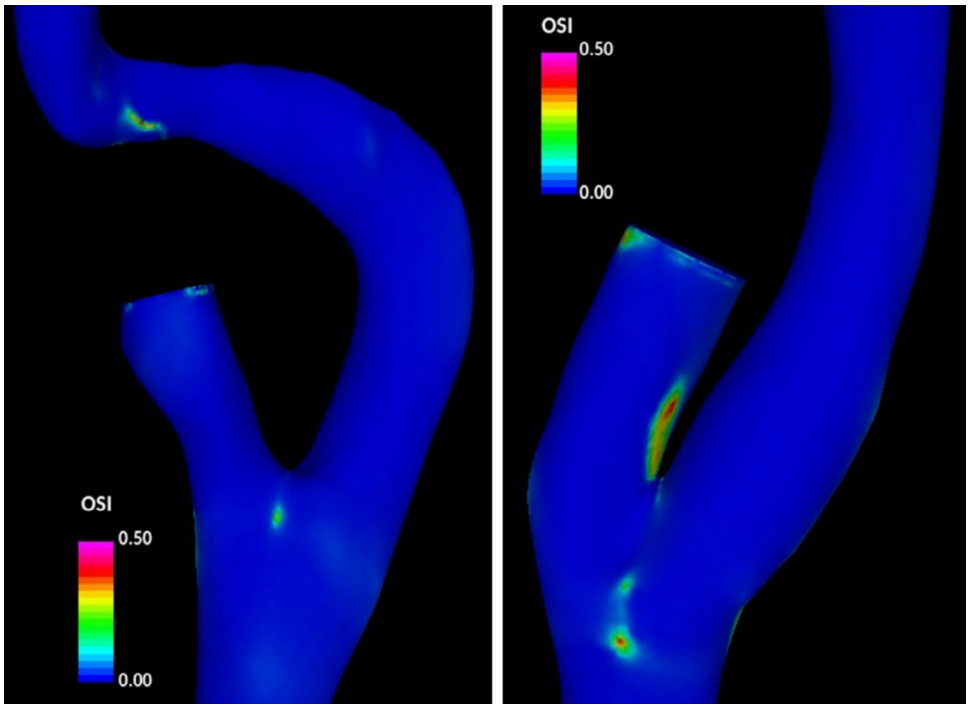

FIGURE 7 | Oscillatory shear index (OSI) in the left bulb of patient 1 (left) and patient 2 (right).

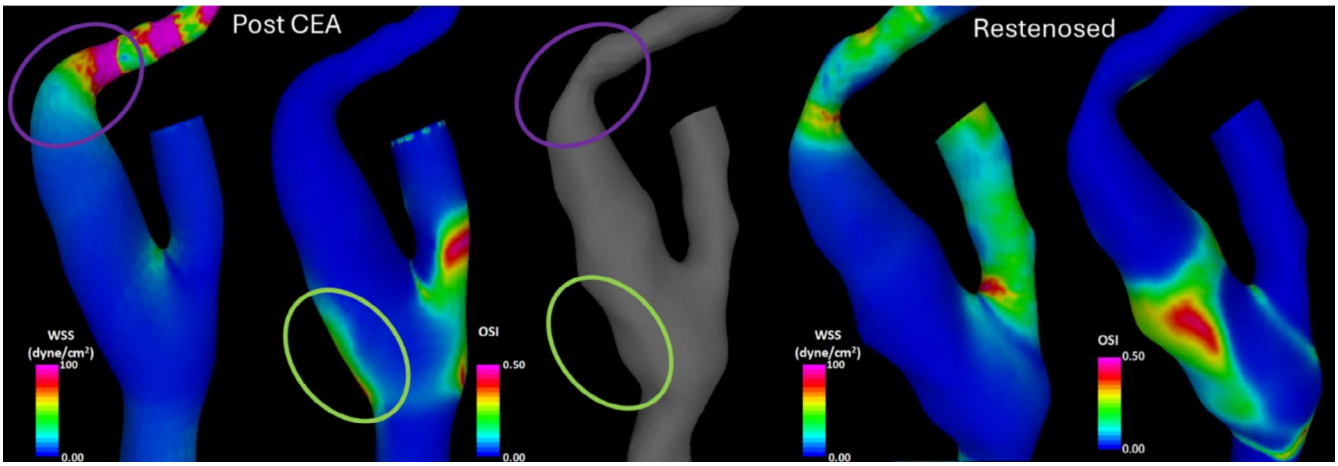

FIGURE 8 | Peak systole WSS and OSI immediately post-CEA with patch (patient 1), and after restenosis. The ovals indicate the regions where the bulb restenosed.

distensibility, of the vessel wall were unavailable, which limited the ability to model compliance to simply implementing a wall velocity to a rigid vessel as opposed to full fluid–structure interaction simulations. Patient-specific flow rate waveforms were only available in the CCA and ICA, while the ECA only had a mean flow rate measured. This required estimating the ECA waveform from the provided data.

This study also involves simplifying assumptions and limitations common to hemodynamic studies of cerebral blood flow and pathologies such as resolution of the MR imaging and model choices. We employed a Newtonian viscosity model, based on the lack of rheological data and its ability to reasonably capture bulk flow metrics [27]. A Womersley flow profile was prescribed, and while one study found that a parabolic velocity profile produced the most similar results to a patient-specific profile, the study also noted that precise geometric reconstruction and measurement of flow rate waveforms were more imperative for having accurate outcomes [28]. Another possible limitation that has not been studied here is the vessel truncation used for the CCA inlet and ICA/ECA outlets. Finally, certain patient- and intervention-specific factors were not considered, including the suture technique, patch material, physiological, and pathological vessel characteristics such as thickness, elasticity, and atherosclerotic severity.

5 | Conclusions

The right bulb of the patch angioplasty patient, which later restenosed, produced a nonphysiological hemodynamic environment, and the CEA procedure failed to restore the hemodynamic conditions experienced by the healthy, left bulb. In

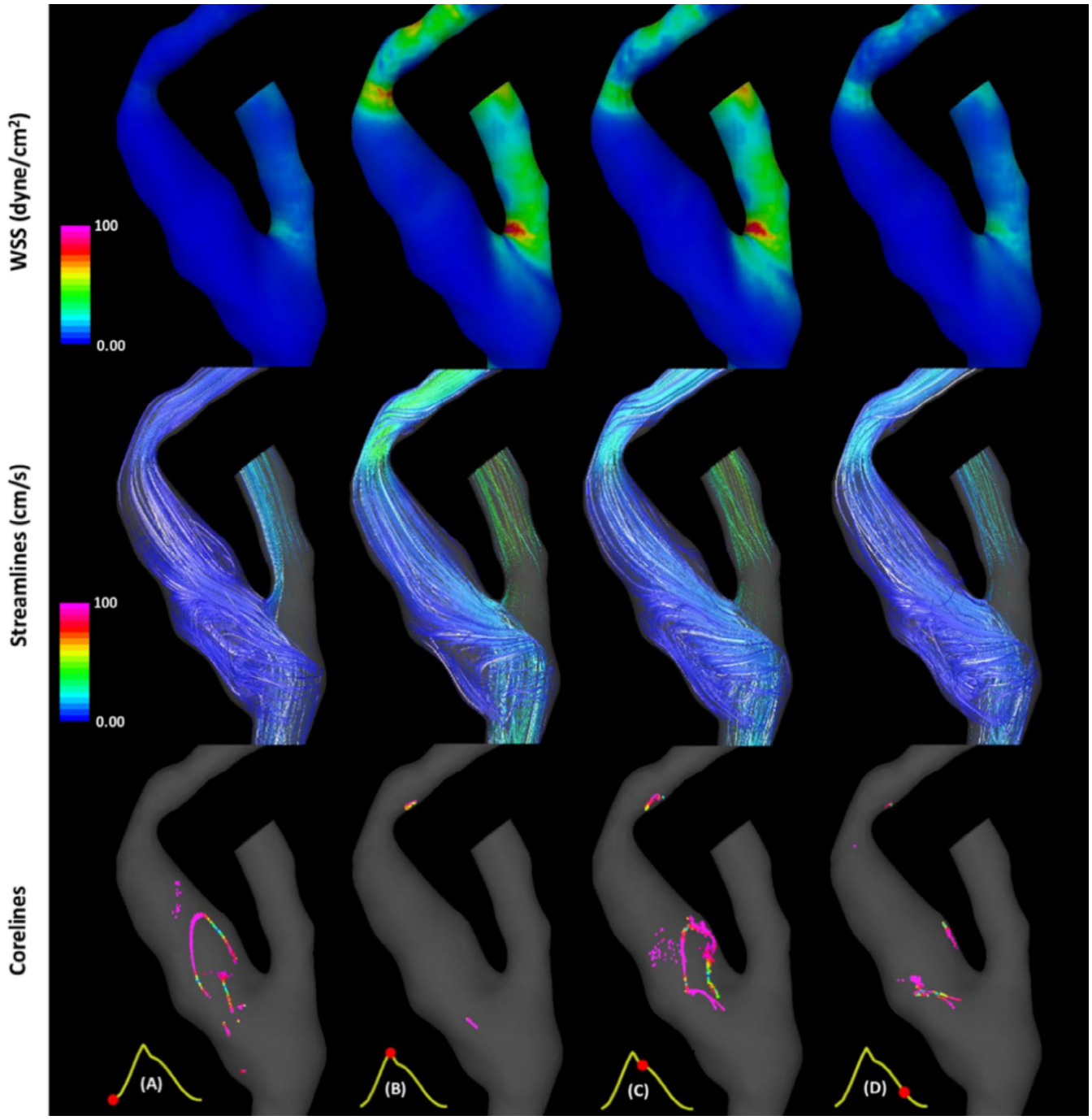

FIGURE 9 | Flow visualization in the right bulb of patient 1 (CEA with patch) after it restenosed.

TABLE 4 | Change in hemodynamic parameters when using contralateral (healthy) flow rates.

Patient	Bulb	WSS	OSI	VOR	CORELEN	KE
Pt1	Right (CEA patch)	0%	0%	8%	14%	12%
Pt2	Right (CEA no patch)	62%	−38%	43%	6%	96%

stark contrast, the primary closure of the right bulb of the other patient created physiological WSS trends and healthy mixing, both of which were also present in the healthy, left bulb. These differences in CEA outcome are thought to be linked to the geometry rendered by the closing method and not directly related to the closing method or prescribed flow characteristics.

TABLE 5 | Change in hemodynamic parameters when using moving wall velocity due to compliance.

Patient	Bulb	WSS	OSI	VOR	CORELEN	KE
Pt1	Left (healthy)	−2%	−37%	0%	−37%	−7%
	Right (CEA patch)	−2%	−13%	−1%	−23%	−8%
Pt2	Left (healthy)	−14%	−49%	−5%	−16%	−32%
	Right (CEA no patch)	−11%	−56%	−1%	−3%	−40%

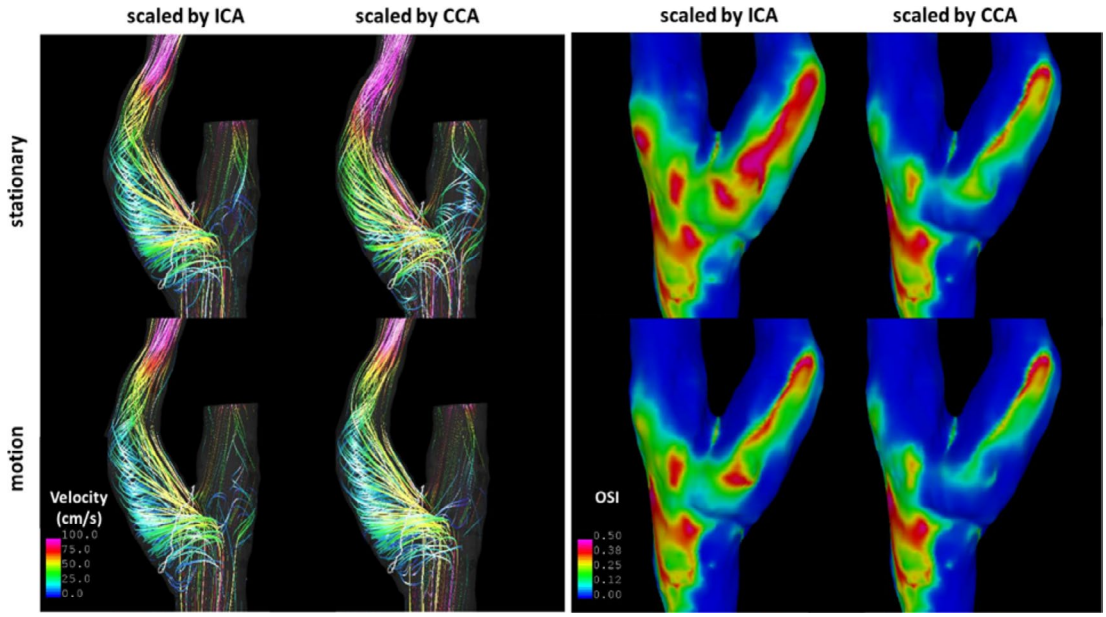

FIGURE 10 | Visualization of flow structures (left) and WSS distributions (right) in patient 2 (larger changes) obtained with rigid wall models (top) and compliant (moving) wall models (bottom), as well as changes obtained with ECA flow curves derived by scaling the ICA or CCA flow waveforms.

TABLE 6 | Change in hemodynamic parameters when using CCA waveform instead of ICA waveform (baseline) for ECA boundary conditions.

Patient	Bulb	WSS	OSI	VOR	CORELEN	KE
Pt1	Left (healthy)	−1%	−17%	0%	−47%	−3%
	Right (CEA patch)	−1%	0%	−1%	−8%	−2%
Pt2	Left (healthy)	−6%	−35%	−3%	−32%	−20%
	Right (CEA no patch)	−10%	−62%	−1%	2%	−35%

TABLE 7 | Change in time-averaged hemodynamic parameters when using steady mean flow rates as boundary conditions.

Patient	Bulb	WSS	VOR	CORELEN	KE
Pt1	Left (healthy)	−2%	−1%	−67%	−19%
	Right (CEA patch)	−2%	−3%	−89%	−17%
Pt2	Left (healthy)	−27%	−7%	103%	−58%
	Right (CEA no patch)	−13%	−1%	−1%	−53%

Ethics Statement

STUDY2024-0962 received IRB approval from the University of Illinois Chicago.

Conflicts of Interest

The authors declare no conflicts of interest.

Data Availability Statement

The computational models and CFD results are available for interested researchers upon request.

References

1. R. W. Hobson, J. E. Goldstein, Z. Jamil, et al., "Carotid Restenosis: Operative and Endovascular Management," *Journal of Vascular Surgery* 29, no. 2 (1999): 228–238, https://doi.org/10.1016/S0741-5214(99)70376-9.

2. A. Muto, T. Nishibe, H. Dardik, and A. Dardik, "Patches for Carotid Artery Endarterectomy: Current Materials and Prospects," *Journal of Vascular Surgery* 50, no. 1 (2009): 206–213, https://doi.org/10.1016/j.jvs.2009.01.062.

3. S. Orrapin, T. Benyakorn, B. Siribumrungwong, and K. Rerkasem, "Patch Angioplasty Versus Primary Closure for Carotid Endarterectomy," *Cochrane Database of Systematic Reviews* 8, no. 8 (2022): CD000160, https://doi.org/10.1002/14651858.CD000160.PUB4.

4. T. İyigün, M. Kyaruzi, B. Timur, M. İyigün, and Ü. Aydın, "Our Midterm Restenosis Results Using Patch Angioplasty Closure Versus Primary Closure in Patients Undergoing Carotid Endarterectomy: A Comparative Study," *Turkish Journal of Vascular Surgery* 28, no. 1 (2019): 19–23, https://doi.org/10.9739/tjvs.2019.237.

5. S. Wu, H. Wang, J. Guo, et al., "Comparative on the Effectiveness and Safety of Different Carotid Endarterectomy Techniques: A Single-Center Retrospective Study," *Journal of Cardiothoracic Surgery* 19, no. 1 (2024): 1–9, https://doi.org/10.1186/S13019-024-02838-0/TABLES/4.

6. A. M. Malek, S. L. Alper, and S. Izumo, "Hemodynamic Shear Stress and Its Role in Atherosclerosis," *JAMA* 282, no. 21 (1999): 2035–2042, https://doi.org/10.1001/JAMA.282.21.2035.

7. N. A. Buchmann, M. C. Jermy, and C. V. Nguyen, "Experimental Investigation of Carotid Artery Haemodynamics in an Anatomically Realistic Model," *International Journal of Experimental and Computational Biomechanics* 1, no. 2 (2009): 172, https://doi.org/10.1504/IJECB.2009.029192.

8. S. W. I. Onwuzu, A. C. Ugwu, G. C. E. Mbah, and I. S. Elo, "Measuring Wall Shear Stress Distribution in the Carotid Artery in an African Population: Computational Fluid Dynamics Versus Ultrasound Doppler Velocimetry," *Radiography* 27, no. 2 (2021): 581–588, https://doi.org/10.1016/J.RADI.2020.11.018.

9. D. N. Ku, D. P. Giddens, C. K. Zarins, and S. Glagov, "Pulsatile Flow and Atherosclerosis in the Human Carotid Bifurcation. Positive Correlation Between Plaque Location and Low Oscillating Shear Stress," *Arteriosclerosis: An Official Journal of the American Heart Association, Inc* 5, no. 3 (1985): 293–302, https://doi.org/10.1161/01.ATV.5.3.293.

10. H. F. Younis, M. R. K. Mofrad, R. C. Chan, et al., "Hemodynamics and Wall Mechanics in Human Carotid Bifurcation and Its Consequences for Atherogenesis: Investigation of Inter-Individual Variation," *Biomechanics and Modeling in Mechanobiology* 3, no. 1 (2004): 17–32, https://doi.org/10.1007/S10237-004-0046-7/FIGURES/8.

11. M. Markl, F. Wegent, T. Zech, et al., "In Vivo Wall Shear Stress Distribution in the Carotid Artery," *Circulation. Cardiovascular Imaging* 3, no. 6 (2010): 647–655, https://doi.org/10.1161/CIRCIMAGING.110.958504.

12. A. Raptis, P. Tasso, K. Batzalexis, et al., "Remodeling Effects of Carotid Artery Stenting Versus Endarterectomy With Patch Angioplasty in Terms of Morphology and Hemodynamics," *Computers in Biology and Medicine* 140 (2022): 105072, https://doi.org/10.1016/J.COMPBIOMED.2021.105072.

13. X. Zhou, L. Yin, L. Xu, and F. Liang, "Non-Periodicity of Blood Flow and Its Influence on Wall Shear Stress in the Carotid Artery Bifurcation: An In Vivo Measurement-Based Computational Study," *Journal of Biomechanics* 101 (2020): 109617, https://doi.org/10.1016/j.jbiomech.2020.109617.

14. J. M. Dolan, J. Kolega, and H. Meng, "High Wall Shear Stress and Spatial Gradients in Vascular Pathology: A Review," *Annals of Biomedical Engineering* 41, no. 7 (2013): 1411–1427, https://doi.org/10.1007/s10439-012-0695-0.

15. H. Ha, W. Choi, H. Park, and S. J. Lee, "Effect of Swirling Blood Flow on Vortex Formation at Post-Stenosis," *Proceedings of the Institution of Mechanical Engineers* 229, no. 2 (2015): 175–183, https://doi.org/10.1177/0954411915573065.

16. T. Fukushima, T. Homma, K. Harakawa, N. Sakata, and T. Azuma, "Vortex Generation in Pulsatile Flow Through Arterial Bifurcation Models Including the Human Carotid Artery," *Journal of Biomechanical Engineering* 110, no. 3 (1988): 166–171, https://doi.org/10.1115/1.3108426.

17. S. W. Lee, L. Antiga, J. D. Spence, and D. A. Steinman, "Geometry of the Carotid Bifurcation Predicts Its Exposure to Disturbed Flow," *Stroke* 39, no. 8 (2008): 2341–2347, https://doi.org/10.1161/STROKEAHA.107.510644.

18. M. Domanin, D. Gallo, C. Vergara, P. Biondetti, L. V. Forzenigo, and U. Morbiducci, "Prediction of Long Term Restenosis Risk After Surgery in the Carotid Bifurcation by Hemodynamic and Geometric Analysis," *Annals of Biomedical Engineering* 47, no. 4 (2019): 1129–1140, https://doi.org/10.1007/s10439-019-02201-8.

19. G. Bertoletti, A. Varroni, M. Misuraca, M. Massucci, and A. Pacelli, "Carotid Artery Diameters, Carotid Endarterectomy Techniques and Restenosis," *Journal of Vascular Medicine and Surgery* 1, no. 3 (2013): 114, https://doi.org/10.4172/2329-6925.1000114.

20. D. C. Baeriswyl, I. Prionisti, T. Peach, et al., "Disturbed Flow Induces a Sustained, Stochastic NF-κB Activation Which May Support Intracranial Aneurysm Growth In Vivo," *Scientific Reports* 9, no. 1 (2019): 4738, https://doi.org/10.1038/s41598-019-40959-y.

21. J. R. Cebral, M. A. Castro, S. Appanaboyina, C. M. Putman, D. Millan, and A. F. Frangi, "Efficient Pipeline for Image-Based Patient-Specific Analysis of Cerebral Aneurysm Hemodynamics: Technique and Sensitivity," *IEEE Transactions on Medical Imaging* 24, no. 4 (2005): 457–467, https://doi.org/10.1109/TMI.2005.844159.

22. J. R. Cebral, P. J. Yim, R. Löhner, O. Soto, and P. L. Choyke, "Blood Flow Modeling in Carotid Arteries With Computational Fluid Dynamics and MR Imaging," *Academic Radiology* 9, no. 11 (2002): 1286–1299, https://doi.org/10.1016/S1076-6332(03)80562-7.

23. R. Löhner, J. Cebral, and S. Appanaboyina, "Parabolic Recovery of Boundary Gradients," *Communications in Numerical Methods in Engineering* 24, no. 12 (2008): 1611–1615, https://doi.org/10.1002/CNM.1054.

24. R. Löhner, C. Yang, J. Cebral, F. Camelli, O. Soto, and J. Waltz, "Improving the Speed and Accuracy of Projection-Type Incompressible Flow Solvers," *Computer Methods in Applied Mechanics and Engineering* 195, no. 23–24 (2006): 3087–3109, https://doi.org/10.1016/J.CMA.2004.07.058.

25. F. Mut, M. Lawson, and J. Cebral, "Differences in Parent Artery Geometry Between ACOM and MCA aneUrysms," (2019), Summer Biomech. Bioeng. Biotransport Conf. SB3C2019.

26. G. Byrne, F. Mut, and J. Cebral, "Quantifying the Large-Scale Hemodynamics of Intracranial Aneurysms," *American Journal of Neuroradiology* 35, no. 2 (2014): 333–338, https://doi.org/10.3174/AJNR.A3678.

27. U. Morbiducci, D. Gallo, D. Massai, et al., "On the Importance of Blood Rheology for Bulk Flow in Hemodynamic Models of the Carotid Bifurcation," *Journal of Biomechanics* 44, no. 13 (2011): 2427–2438, https://doi.org/10.1016/J.JBIOMECH.2011.06.028.

28. I. C. Campbell, J. Ries, S. S. Dhawan, A. A. Quyyumi, W. R. Taylor, and J. N. Oshinski, "Effect of Inlet Velocity Profiles on Patient-Specific Computational Fluid Dynamics Simulations of the Carotid Bifurcation," *Journal of Biomechanical Engineering* 134, no. 5 (2012): 051001, https://doi.org/10.1115/1.4006681.